



A NIR-driven photocatalyst based on α -NaYF₄:Yb,Tm@TiO₂ core–shell structure supported on reduced graphene oxide

Wanjun Wang^a, Yecheng Li^a, Zhiwen Kang^b, Feng Wang^b, Jimmy C. Yu^{a,*}

^a Department of Chemistry and Institute of Environment, Energy and Sustainability, The Chinese University of Hong Kong, Shatin, N.T., Hong Kong, China

^b Department of electronic engineering, The Chinese University of Hong Kong, Shatin, N.T., Hong Kong, China

ARTICLE INFO

Article history:

Received 2 July 2015

Received in revised form 18 August 2015

Accepted 11 September 2015

Available online 16 September 2015

Keywords:

Photocatalysis

Near-infrared-light

NaYF₄

TiO₂

Graphene

Organic pollutants degradation

ABSTRACT

The development of near-infrared (NIR) light-driven photocatalysts is needed to utilize the large portion of NIR energy in sunlight. In this work, a new strategy to fabricate advanced upconversion-based NIR-driven photocatalysts was developed by integrating core–shell nanostructure of α -NaYF₄:Yb,Tm@TiO₂ with reduced graphene oxide (RGO) nanosheets. This new α -NaYF₄:Yb,Tm@TiO₂/RGO composite was synthesized by a facile wet chemical method. The product exhibited significantly enhanced photocatalytic activity than bare α -NaYF₄:Yb,Tm@TiO₂ and α -NaYF₄:Yb,Tm/TiO₂/RGO physical mixture for the degradation of various organic pollutants, including methylene blue (MB), methyl orange (MO) and phenol, under NIR (980 nm laser) irradiation. Highly reactive hydroxyl radicals (\cdot OH) were found to be the major reactive species. It was revealed that the core–shell structure of α -NaYF₄:Yb,Tm@TiO₂ improved the upconversion UV energy transfer, while the incorporation of RGO facilitated the photo-generated $e^- - h^+$ separation after excited by the upconversion energy. Our discovery highlights the potential of developing NIR-driven photocatalysts by taking advantage of the synergic effects of core–shell upconversion materials combined with graphene for environmental and energy-related applications.

© 2015 Elsevier B.V. All rights reserved.

1. Introduction

Semiconductor photocatalysis has attracted worldwide attention due to its potential in solar energy conversion to resolve the energy and environmental-related problems [1]. Especially, TiO₂-based heterogeneous photocatalysis is considered particularly attractive because TiO₂ is widely available, inexpensive, non-toxic and has relatively high chemical stability [2,3]. However, TiO₂ is only active under UV-light irradiation due to its wide band gap ($E_g = 3.2$ eV for anatase), resulting in a low photo-electronic transition efficiency since UV radiation accounts for only 5% of the total solar spectrum [4]. Therefore, efforts have been devoted to modify TiO₂ to extend the light absorption region and increase the quantum efficiency. These include noble metal deposition [5], metallic/nonmetallic ion doping [6], heterojunctions formation [7] and crystal vacancy engineering [8,9]. Up to date, most of the studies have focused on the utilization of visible light (VL) region, as it constitutes about 48% of solar spectrum [10]. However, studies aimed at utilizing near-infrared (NIR) light, despite the fact that NIR accounts for about 44% of solar spectrum, are rather limited

compared with the abundant studies on visible-light-driven photocatalysis.

Lanthanide-doped materials are known as efficient luminescent materials due to their narrow emission bands, long luminescence lifetimes, as well as their physical and chemical stability [11]. Moreover, when doped with appropriate ions, they can convert NIR excitation light into visible or UV emission light, which then excites corresponding photocatalysts [12]. Yb,Tm-codoped fluoride, such as YF₃ and NaYF₄, are typical upconversion materials used in NIR-driven photocatalysis. For example, Qin et al. has reported the photocatalytic activity of YF₃:Yb,Tm/TiO₂ and NaYF₄:Yb,Tm/TiO₂ under NIR light irradiation [13,14]. Meanwhile, graphene and its counterpart, reduced graphene oxide (RGO), have emerged as attractive candidates for constructing graphene-based materials because of their remarkable electrical conductivity, large specific surface area and high chemical stability [15–17]. On account of these favorable properties, graphene has been extensively utilized in electrochemistry, solar cells, thermomechanics, nanoelectronics, and also provides new opportunities for photocatalyst carriers and promoter. A variety of studies have revealed that the incorporation of graphene with semiconductors exhibits enhanced photocatalytic activity under either UV or VL-irradiation [18–20]. However, little attention has been paid to the function of graphene in NIR-driven photocatalysis.

* Corresponding author. Fax: +852 2603 5057.

E-mail address: jimyu@cuhk.edu.hk (J.C. Yu).

In general, the upconversion-based NIR-driven photocatalysis has at least two major challenges that lead to the usually low photocatalytic efficiency. One is how to efficiently utilize the valuable upconversion energy transferred from the excited upconversion core. This may be realized by constructing core–shell structure which can protect the upconversion core from surface quenching and increase the energy transfer efficiency to the photocatalyst shell [21–23]. The other is how to suppress the photo-generated $e^- - h^+$ recombination of the photocatalyst after excited by upconversion energy. The graphene/RGO is expected to serve as an electron collector and transporter to accept and shuttle electrons generated from the semiconductors, thus preventing recombination and prolonging lifetime of the photo-generated $e^- - h^+$ pairs [24]. In this regard, YF_3 :Yb,Tm/P25/graphene [25] and β -NaYF₄:Yb,Tm/N-P25/ graphene [26] composites have been reported, but the individual components (i.e. upconversion materials, P25–TiO₂ and graphene) are only physically mixed without well-defined nanostructures. As a result, the photocatalytic activity under NIR is relatively low and unsatisfactory.

Herein, we combined the above-mentioned strategies together and demonstrated for the first time a α -NaYF₄:Yb,Tm@TiO₂ core–shell structure supported on RGO as a new NIR-driven photocatalyst. A facile wet-chemical synthetic route was developed to *in situ* grow crystalline TiO₂ shell on the α -NaYF₄:Yb,Tm core, followed by embedding the α -NaYF₄:Yb,Tm@TiO₂ submicrospheres on RGO nanosheets. The as-prepared α -NaYF₄:Yb,Tm@TiO₂/RGO composites exhibit improved photoelectrochemical performance as well as significantly higher NIR-driven photocatalytic organic pollutants (i.e. methylene blue, methyl orange and phenol) degradation activity than that of bare α -NaYF₄:Yb,Tm@TiO₂ and α -NaYF₄:Yb,Tm/TiO₂/RGO physical mixture. As a proof of concept, this work provides new insights for the development of NIR-driven photocatalysis by incorporation of core–shell upconversion photocatalyst with graphene.

2. Experimental

2.1. Materials

All the chemicals and reagents are of analytical grade. Y₂O₃ (Aldrich, 99.99%), Yb₂O₃ (Meryer, 99.99%), Tm₂O₃ (Meryer, 99.99%), NaF (Riedel-deHaen, 99%), Ethylenediaminetetraacetic acid disodium salt (EDTA, BDH Chemicals, 99.5%), Polyvinylpyrrolidone (PVP K-30, Aldrich), Triton X-100 (Aldrich), Titanium n-butoxide (TBOT, Aldrich, 99%), Isopropanol (BDH Chemicals, 99.7%), benzoquinone (International Laboratory USA, 99%) were purchased and used without further purification. Fe(II)-EDTA solution was prepared by dissolving equal mole ratio of FeSO₄ (Ajax Chemicals) and EDTA in water, and stored in refrigerator at $\sim 4^\circ\text{C}$. Graphene oxide (GO) was prepared by a modified Hummer method according to our previous report [27].

2.2. Sample preparation

2.2.1. Synthesis of α -NaYF₄:Yb,Tm submicrospheres

The rare earth (RE) nitrates were obtained by dissolving the RE oxides Y₂O₃, Yb₂O₃, and Tm₂O₃ with a stoichiometric ratio of 79.5:20.0:5 in nitric acid, followed by heating the solution to evaporate the water completely. The α -NaYF₄:Yb,Tm submicrospheres with diameters of 100–200 nm were synthesized via a modified EDTA-assisted hydrothermal method [28]. Briefly, RE(NO₃)₃, EDTA and NaF with molar ratio of 1:1:4 was put in 16 mL deionized water. After stirring for 1 h, the white suspension was transferred into a 20 mL Teflon-lined stainless steel autoclave and heated to 180°C

for 2 h. The resulting product was collected by centrifuged, washed with deionized water and dried at 60°C overnight.

2.2.2. Synthesis of α -NaYF₄:Yb,Tm@TiO₂

The α -NaYF₄:Yb,Tm@TiO₂ core–shell composite was prepared by a PVP-assisted surface coating [13,23] and hydrothermal crystallization method. The whole synthetic route was shown in Fig. 1. In a typical synthesis, 50 mg α -NaYF₄:Yb,Tm was dispersed in 1 mL 0.2 g/mL PVP solution under ultrasonication to form a homogeneous white suspension. Then 0.2 mL TBOT in ethanol was added to the solution under vigorous stirring for 1 h. To produce crystalline TiO₂ shell, the above precursor solution was transferred to a 20 mL Teflon-lined stainless steel autoclave and heated to 160°C for 6 h. After cooling to room temperature, the resulting α -NaYF₄:Yb,Tm@TiO₂ was collected by centrifugation and washed with H₂O/ethanol several times, then dried at 60°C in air.

2.2.3. Synthesis of α -NaYF₄:Yb,Tm@TiO₂/RGO

To produce α -NaYF₄:Yb,Tm@TiO₂/RGO, the as-prepared α -NaYF₄:Yb,Tm@TiO₂ was dispersed in 30 mL H₂O with 0.4 mL 1% TX-100 under ultrasonication, followed by dropwisely adding 0.6 mL GO solution (1 mg/mL) under vigorous stirring at 60°C . After stirring for 0.5 h, the resulting product was collected by centrifuged, and then redispersed in 30 mL H₂O. Finally, the suspension containing α -NaYF₄:Yb,Tm@TiO₂/GO was irradiated under a 300 W Xenon lamp (Beijing Perfect Light Co. Ltd., Beijing) for 2 h under Ar aeration. After the photo-reduction of GO to RGO, the α -NaYF₄:Yb,Tm@TiO₂/RGO were obtained by centrifuged, washed with deionized water and dried at 60°C in air. As a comparison, α -NaYF₄:Yb,Tm/RGO was prepared by the same procedure with the absence of TiO₂, and α -NaYF₄:Yb,Tm/TiO₂/RGO mixture was prepared by mechanically mixing the same ratio of α -NaYF₄:Yb,Tm, TiO₂ and RGO, which were synthesized according to the above procedure. The weight ratio in the α -NaYF₄:Yb,Tm@TiO₂/RGO composites was obtained by elemental analysis (48.65 wt% α -NaYF₄:Yb,Tm; 47.48 wt% TiO₂; 3.87 wt% RGO).

2.3. Characterizations

X-Ray diffraction (XRD) patterns were recorded with a Rigaku SmartLab X-ray diffractometer using Cu K α 1 irradiation ($\lambda = 1.5406 \text{ \AA}$). The accelerating voltage and applied current were 40 kV and 40 mA, respectively. UV-vis diffuse reflectance spectra (UV-vis DRS) of the powders were obtained for the dry-pressed disk samples using a Varian Cary 500 UV-vis spectrophotometer equipped with a labsphere diffuse reflectance accessory. BaSO₄ was used as a reflectance standard in the UV-vis DRS experiment. The general morphologies of the products were characterized by scanning electron microscopy (FESEM, FEI, Quanta 400 FEG) equipped with an energy-dispersive X-ray (EDX) spectrometer, and transmission electron microscopy (TEM, FEI Tecnai G2 Spirit). The high-resolution transmission electron microscopy (HRTEM) was obtained on a FEI Tecnai F20 transmission electron microscopy operated at 200 kV. Elemental analysis was conducted by inductively coupled plasma optical emission spectrometer (ICP-OES, PerkinElmer Optima 4300 DV). Photoluminescence (PL) spectra were recorded at room temperature with a fiber coupled spectrometer (Ocean Optics 2000) with excitation of a 980 nm diode laser (Lumics, LU0975M400). Photoelectrochemical measurements of the samples were carried out on an electrochemical workstation (CHI 660D, Shanghai Chen Hua Instrument Company, China) with a conventional three electrode cell, using a Pt plate and a saturated Ag/AgCl electrode as counter electrode and reference electrode, respectively. The working electrode was prepared on indium-tin oxide (ITO) glasses, which was cleaned by sonication in chloroform, acetone and ethanol for 30 min, respectively. The glass

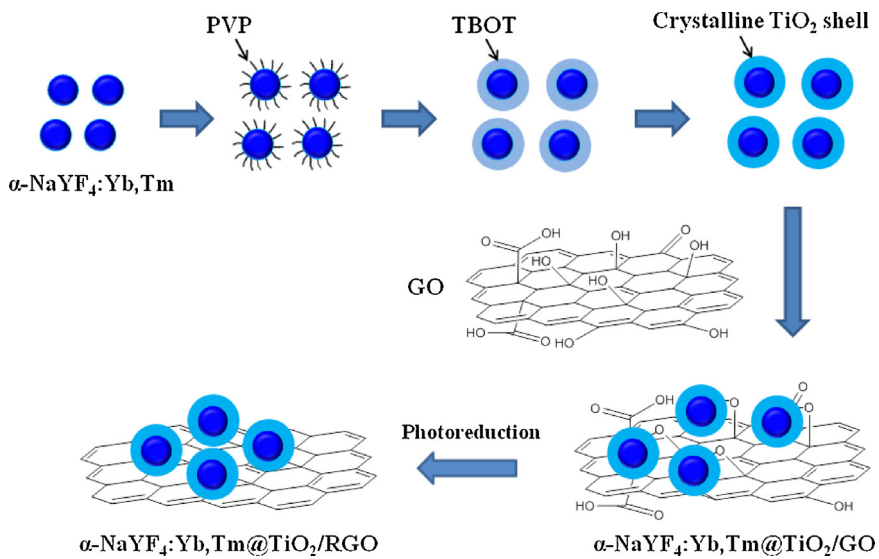


Fig. 1. Schematic illustration of the synthesis process of $\alpha\text{-NaYF}_4\text{:Yb,Tm@TiO}_2\text{/RGO}$ composites.

was then rinsed with water and kept in isopropanol for 24 h. Five-milligrams of samples and 10 μL of Nafion solution (5 wt%) were dispersed in a 1 mL water/isopropanol mixed solvent (3:1 v/v) by sonication to form a homogeneous catalyst colloid. Then, 100 μL of the catalyst colloid was deposited onto the ITO glass with areas of about 1 cm^2 . The working electrodes were immersed in a 0.1 M Na_2SO_4 aqueous solution without additive for 30 s before measurement was carried out. Electrochemical impedance spectroscopy (EIS) displayed as a Nyquist plot was carried out in the frequency range of 0.05 Hz– 10^5 Hz with an AC perturbation signal of 5 mV. Total organic carbon (TOC) analysis was conducted by auto-sampler ASI-V connecting to the TOC analyzer TOC-V_{CSH/CSN} (Shimadzu Corporation, Kyoto, Japan). The generation of $\cdot\text{OH}$ was investigated through the method of photoluminescence with terephthalic acid. The $\cdot\text{OH}$ was captured by terephthalic acid to produce a fluorescent product 2-hydroxyterephthalic acid [29] and then analyzed by a fluorescence spectrophotometer (Hitachi F-4500, excitation wavelength: 320 nm; fluorescence peak: 425 nm).

2.4. Photocatalytic activity measurements

The NIR-driven photocatalytic activity for organic pollutants degradation was evaluated by measuring the photodegradation of methylene blue (MB), methyl orange (MO) and phenol as the standard pollutants. In a typical measurement, 5 mg photocatalysts were suspended in 5 mL of MB (10 ppm), MO (15 ppm) or phenol (20 ppm) aqueous solution in a small glass bottle. The solution was stirred in dark for 1 h to achieve the equilibrium adsorption. Then the suspension was illuminated with a 2 W 980 nm diode laser. After irradiation for a designated time, 1 mL of the pollutants aqueous suspension was taken out and centrifuged. The resulting supernatants were used for UV-vis absorbance measurements at 664, 464 and 269 nm for MB, MO and phenol, respectively. Then the tested supernatants and centrifuged photocatalysts were resuspended by ultrasonication, and put back into the reactor. The photocatalytic activity was analyzed by the time profiles of C/C_0 , where C is the concentration of pollutants at the irradiation time t and C_0 is the concentration in the absorption equilibrium of the photocatalysts before irradiation, respectively. Simulated sun light-driven and NIR-driven photocatalysis were also performed by using a 300 W xenon lamp with an AM 1.5 filter and a long-pass cutoff filter ($\lambda > 700$ nm).

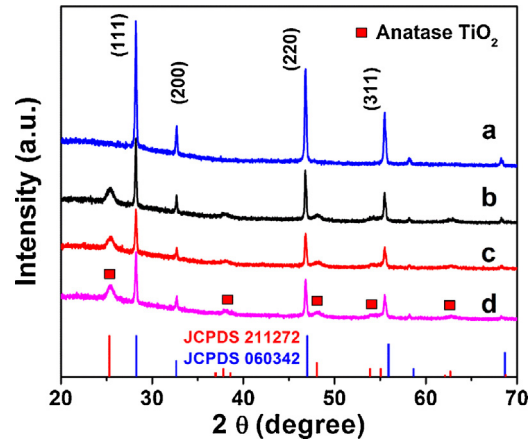


Fig. 2. X-Ray diffraction (XRD) patterns of (a) $\alpha\text{-NaYF}_4\text{:Yb,Tm}$, (b) $\alpha\text{-NaYF}_4\text{:Yb,Tm@TiO}_2$, (c) $\alpha\text{-NaYF}_4\text{:Yb,Tm/TiO}_2\text{/RGO}$ mixture and (d) $\alpha\text{-NaYF}_4\text{:Yb,Tm@TiO}_2\text{/RGO}$.

3. Results and discussion

3.1. Structure and morphology

Fig. 2 presents the XRD patterns of the as-prepared samples. For the $\alpha\text{-NaYF}_4\text{:Yb,Tm}$ sample, the position and relative intensity of all diffraction peaks can be readily indexed to the pure cubic NaYF_4 according to the JCPDS file NO. 06-0342. No impurity peaks can be identified from the XRD pattern, indicating that the as-synthesized $\alpha\text{-NaYF}_4\text{:Yb,Tm}$ is single-phased. After coating with TiO_2 , the XRD pattern exhibits the mixed phase of $\alpha\text{-NaYF}_4\text{:Yb,Tm}$ and anatase TiO_2 , confirming that TiO_2 is successfully coated on the $\alpha\text{-NaYF}_4\text{:Yb,Tm}$. For the $\alpha\text{-NaYF}_4\text{:Yb,Tm@TiO}_2\text{/RGO}$ composite and the $\alpha\text{-NaYF}_4\text{:Yb,Tm/TiO}_2\text{/RGO}$ mixture, the diffraction peaks match well to those of $\alpha\text{-NaYF}_4\text{:Yb,Tm@TiO}_2$, suggesting that the presence of RGO in the hybrids does not disturb the crystallinity of $\alpha\text{-NaYF}_4\text{:Yb,Tm@TiO}_2$. Elemental analysis by ICP-OES shows that the $\alpha\text{-NaYF}_4\text{:Yb,Tm@TiO}_2\text{/RGO}$ composite contains 5.91 wt% Na, 18.56 wt% Y, 4.41 wt% Yb, 0.52 wt% Tm and 28.49 wt% Ti, corresponding to 48.65 wt% $\alpha\text{-NaYF}_4\text{:Yb,Tm}$ and 47.48 wt% TiO_2 , and therefore, the RGO content is about 3.87 wt%. No diffraction peaks corresponding to either RGO or GO can be observed in the XRD pattern of the $\alpha\text{-NaYF}_4\text{:Yb,Tm@TiO}_2\text{/RGO}$ composite,

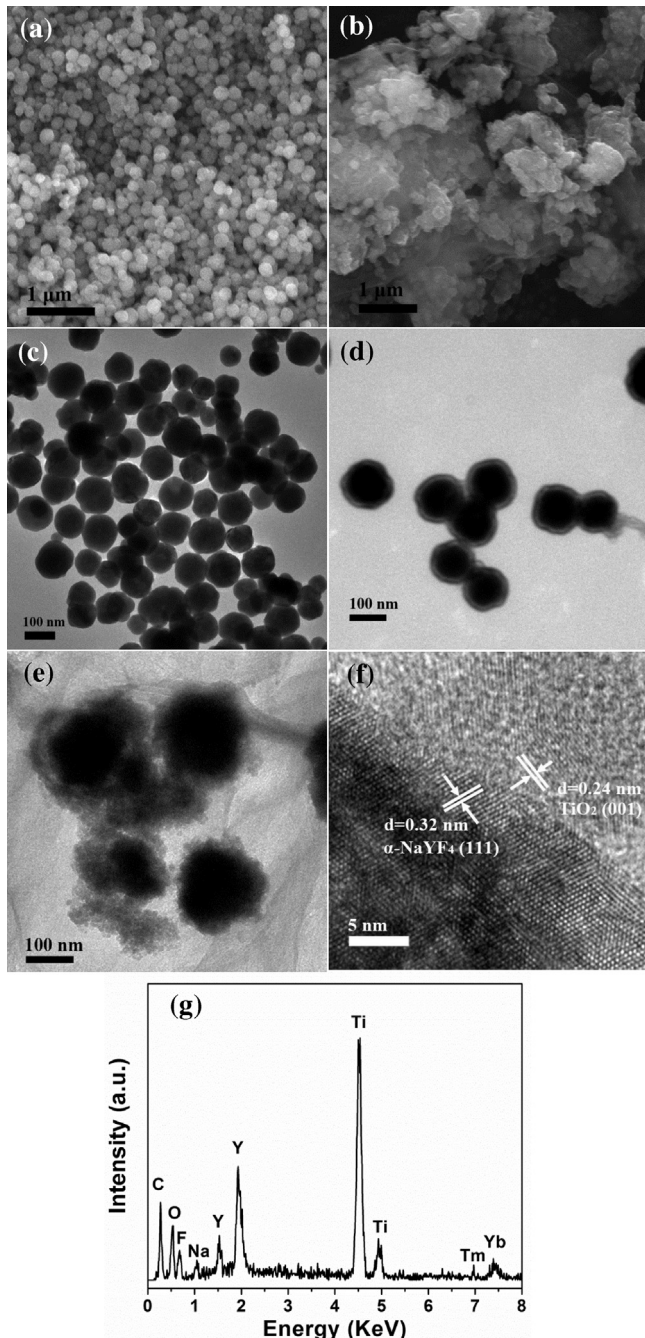


Fig. 3. Scanning electron microscopy (SEM) images of (a) $\alpha\text{-NaYF}_4\text{:Yb,Tm}$ and (b) $\alpha\text{-NaYF}_4\text{:Yb,Tm@TiO}_2\text{/RGO}$; Transmission electron microscopy (TEM) images of (c) $\alpha\text{-NaYF}_4\text{:Yb,Tm}$, (d) $\alpha\text{-NaYF}_4\text{:Yb,Tm@TBOT}$ and (e) $\alpha\text{-NaYF}_4\text{:Yb,Tm@TiO}_2\text{/RGO}$; (f) HRTEM image and (g) energy-dispersive X-ray (EDX) spectrum of $\alpha\text{-NaYF}_4\text{:Yb,Tm@TiO}_2\text{/RGO}$.

which can be attributed to the low content and relatively low diffraction intensity of RGO or GO [30]. The Raman spectra of $\alpha\text{-NaYF}_4\text{:Yb,Tm@TiO}_2\text{/RGO}$ composite clearly shows two characteristic peaks of graphene, which centers at $\sim 1340\text{ cm}^{-1}$ (D bands) and $\sim 1590\text{ cm}^{-1}$ (G bands) respectively (Fig. S1). The D/G intensity ratio is decreased from 0.97 to 0.82, indicating the successful reduction of GO to RGO in the composite [31,32].

The morphology of the as-prepared samples was characterized by SEM and TEM, as shown in Fig. 3. The naked $\alpha\text{-NaYF}_4\text{:Yb,Tm}$ shows submicro-spherical morphology with sizes of about 100 nm in diameter (Fig. 3a and c). With the addition

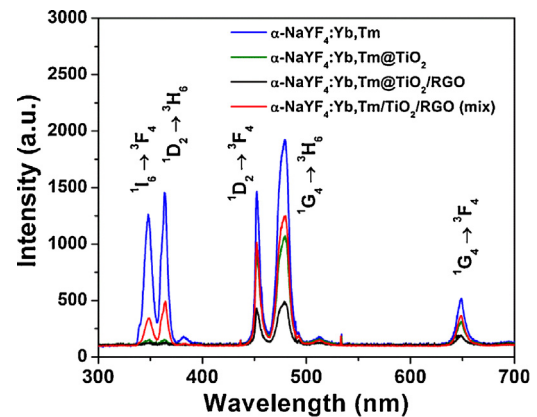


Fig. 4. Upconversion PL spectra of $\alpha\text{-NaYF}_4\text{:Yb,Tm}$, $\alpha\text{-NaYF}_4\text{:Yb,Tm@TiO}_2$, $\alpha\text{-NaYF}_4\text{:Yb,Tm@TiO}_2\text{/RGO}$ and $\alpha\text{-NaYF}_4\text{:Yb,Tm/TiO}_2\text{/RGO}$ mixture under 980 nm excitation at room temperature.

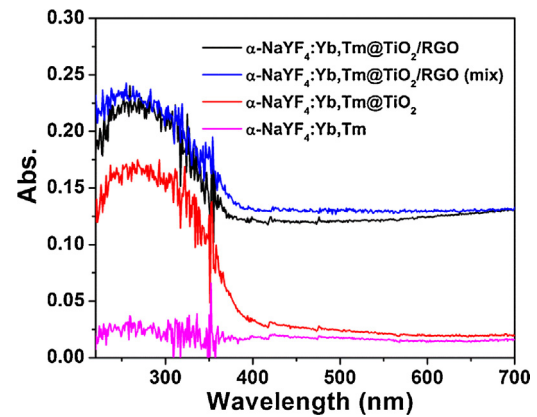


Fig. 5. UV-vis diffuse reflectance spectra (UV-vis DRS) of the as-prepared samples.

of TBOT into the $\alpha\text{-NaYF}_4\text{:Yb,Tm}$ solution, an amorphous TiO_2 shell was evidently deposited around the $\text{NaYF}_4\text{:Yb,Tm}$ submicrospheres (Fig. 3d). After hydrothermal annealing, the amorphous TiO_2 shells were crystallized into nanoparticles. The produced $\alpha\text{-NaYF}_4\text{:Yb,Tm@TiO}_2$ core-shell structure was then supported on the graphene, and the SEM image of $\alpha\text{-NaYF}_4\text{:Yb,Tm@TiO}_2\text{/RGO}$ clearly shows that the $\alpha\text{-NaYF}_4\text{:Yb,Tm@TiO}_2$ submicrospheres are loaded on the high quality ultra-thin graphene layers (Fig. 3b). The detailed core-shell structure supported on graphene is confirmed by TEM observation (Fig. 3e). In addition, the d spacings between the adjacent lattice fringes measured from the HRTEM images are 0.32 nm in the core and 0.24 nm in the shell (Fig. 3f), corresponding to the (1 1 1) planes of cubic $\alpha\text{-NaYF}_4$ and the (0 0 1) planes of anatase TiO_2 , respectively. The EDX spectrum shown in Fig. 3g further confirms that the $\alpha\text{-NaYF}_4\text{:Yb,Tm@TiO}_2\text{/RGO}$ consists of C, O, Na, Y, F, Ti, Yb, Tm elements without any other impurities.

3.2. Optical properties

The NIR-driven photocatalysis depends on the energy transfer from $\alpha\text{-NaYF}_4\text{:Yb,Tm}$ to TiO_2 and RGO. The $\alpha\text{-NaYF}_4\text{:Yb,Tm}$ is a classic upconversion material and shows typical Tm^{3+} photoluminescence (PL) emission characteristics [33–36]. As shown in Fig. 4, under 980 nm laser irradiation, the emission peaks of Tm^{3+} ions at 348 and 364 nm are observed in the UV region, derived from the radioactive transitions of $^1\text{I}_6 \rightarrow ^3\text{F}_4$ and $^1\text{D}_2 \rightarrow ^3\text{H}_6$, respectively. Two blue emission peaks centered at 453 and 478 nm are assigned to $^1\text{D}_2 \rightarrow ^3\text{F}_4$ and $^1\text{G}_4 \rightarrow ^3\text{H}_6$ transitions of Tm^{3+} ions, respectively. The weakest red emission at 648 nm is from

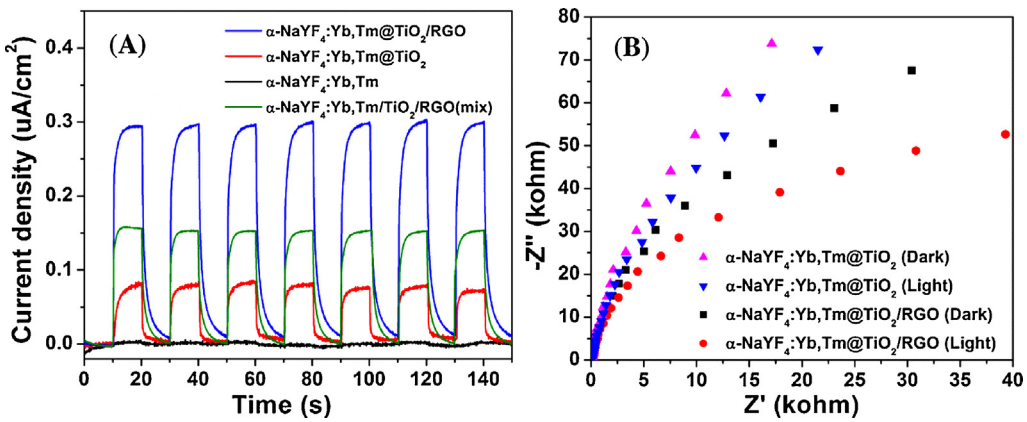


Fig. 6. (A) The transient photocurrent density responses of $\alpha\text{-NaYF}_4\text{:Yb,Tm}$, $\alpha\text{-NaYF}_4\text{:Yb,Tm@TiO}_2$, $\alpha\text{-NaYF}_4\text{:Yb,Tm/TiO}_2\text{/RGO}$ and $\alpha\text{-NaYF}_4\text{:Yb,Tm/TiO}_2\text{/RGO}$ mixture samples electrodes with light on/off cycles under 980 nm laser irradiation; (B) EIS nyquist plots for $\alpha\text{-NaYF}_4\text{:Yb,Tm@TiO}_2$ and $\alpha\text{-NaYF}_4\text{:Yb,Tm@TiO}_2\text{/RGO}$ in 0.1 M Na_2SO_4 solution in the dark and under 980 nm irradiation.

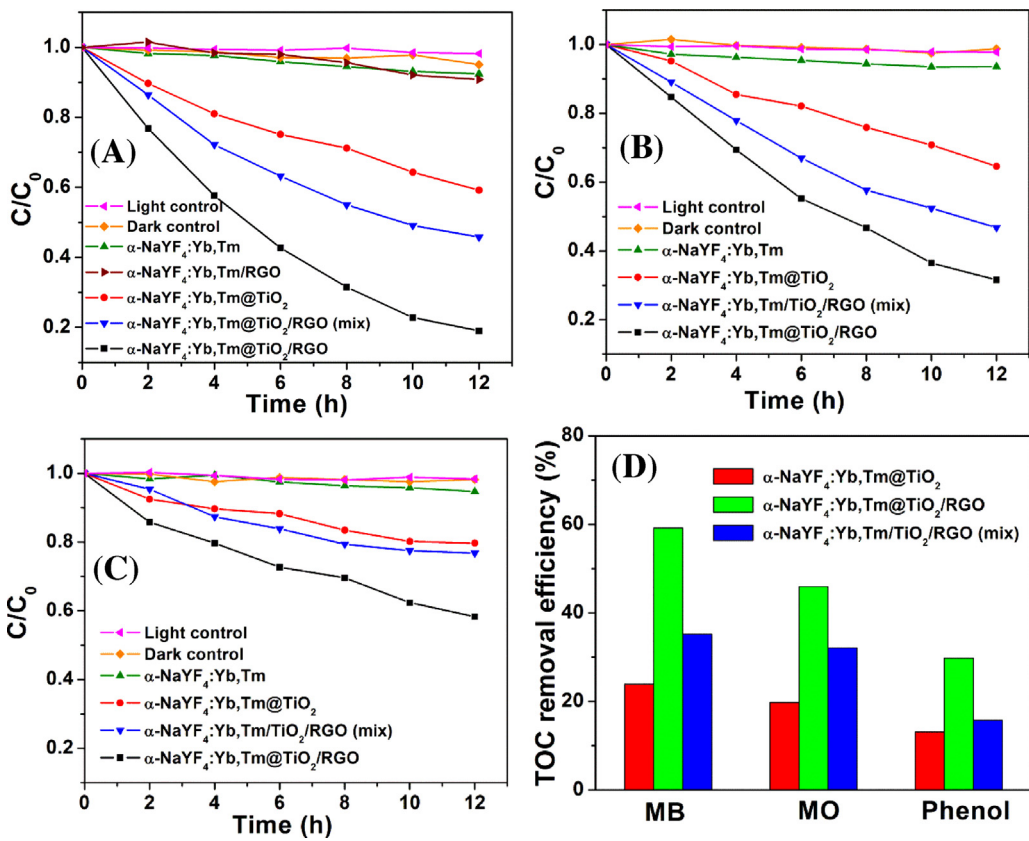


Fig. 7. Concentration changes of (A) MB, (B) MO and (C) phenol in the presence of the as-prepared samples under 980 nm laser irradiation (C_0 : concentration after adsorption); (D) TOC removal efficiency of MB, MO and phenol after NIR irradiation for 12 h in the presence of different samples.

the $^1\text{G}_4 \rightarrow ^3\text{F}_4$ transition. The overall upconversion emissions of the $\alpha\text{-NaYF}_4\text{:Yb,Tm@TiO}_2\text{/RGO}$ are decreased, compared with the bare $\alpha\text{-NaYF}_4\text{:Yb,Tm}$ particles, partially because the incident NIR light is attenuated by the TiO_2 shell and the RGO, which results in a decrease in the excitation light intensity arriving at the $\text{NaYF}_4\text{:Yb,Tm}$ core [37]. However, the intensities of UV emission peaks at ~ 348 nm and ~ 364 nm decrease much more significantly in comparison with that of blue (~ 453 and 478 nm) and red (~ 648 nm) emissions, indicating the upconverted UV energy is absorbed by TiO_2 shell. In addition, the fluorescence intensity ratio of $I_{364\text{nm}}/I_{478\text{nm}}$ for bare $\alpha\text{-NaYF}_4\text{:Yb,Tm}$ is calculated to be 0.78, and this value decreased to 0.19 for the $\alpha\text{-NaYF}_4\text{:Yb,Tm@TiO}_2$. Since the

spectra were recorded under identical conditions and the Tm content was the same, the decrease in $I_{364\text{nm}}/I_{478\text{nm}}$ strongly suggests a UV energy transfer from $\text{NaYF}_4\text{:Yb,Tm}$ to TiO_2 [38]. Furthermore, the UV emission was completely quenched ($I_{364\text{nm}}/I_{478\text{nm}} = 0$) in the case of $\text{NaYF}_4\text{:Yb,Tm@TiO}_2\text{/RGO}$, indicating the incorporation of RGO further improve the energy transfer between $\text{NaYF}_4\text{:Yb,Tm}$ and TiO_2 . However, it is found that the physical mixture of $\alpha\text{-NaYF}_4\text{:Yb,Tm/TiO}_2\text{/RGO}$ shows a $I_{364\text{nm}}/I_{478\text{nm}}$ value of 0.39, which is even larger than that of $\alpha\text{-NaYF}_4\text{:Yb,Tm@TiO}_2$, suggesting the core-shell nanostructure is crucial for the efficient upconversion UV energy transfer.

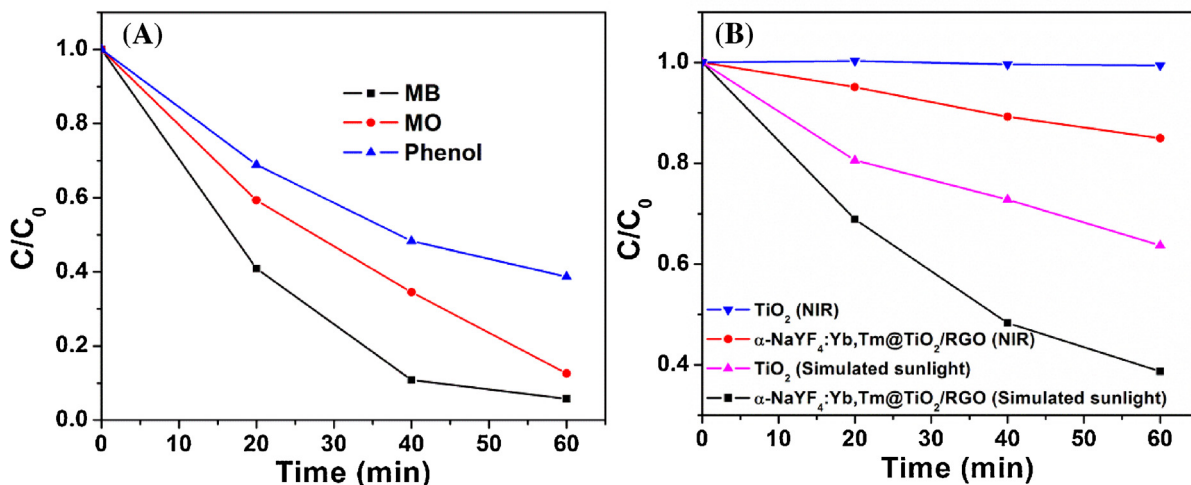


Fig. 8. (A) Photocatalytic degradation of MB, MO and phenol by $\alpha\text{-NaYF}_4\text{:Yb,Tm@TiO}_2\text{/RGO}$ under simulated sunlight (C_0 : concentration after adsorption); (B) comparison of photocatalytic degradation of phenol by TiO_2 and $\alpha\text{-NaYF}_4\text{:Yb,Tm@TiO}_2\text{/RGO}$ under simulated sunlight with cutoff filter ($\lambda > 700 \text{ nm}$).

UV-vis absorption spectra of the as-prepared samples were measured and are shown in Fig. 5. No absorption was found for the bare $\alpha\text{-NaYF}_4\text{:Yb,Tm}$. After coating with the TiO_2 shell, the composites showed a typical 380 nm absorption edge, which overlaps with the $^1\text{I}_6 \rightarrow ^3\text{F}_4$ and $^1\text{D}_2 \rightarrow ^3\text{H}_6$ emission peaks and corresponds to the absorption features of TiO_2 in the UV range, indicating the upconversion energy transfer from $\alpha\text{-NaYF}_4\text{:Yb,Tm}$ to TiO_2 is possible. Moreover, when incorporated with RGO, the $\alpha\text{-NaYF}_4\text{:Yb,Tm@TiO}_2\text{/RGO}$ exhibited even enhanced light absorption in both UV and extended visible region, suggesting the RGO could facilitate the light absorption [39] thus enhance the photocatalytic activity.

3.3. Photoelectrochemical measurements

To reveal the NIR-driven photo-induced charge separation and transfer processes at the photocatalyst electrode interface, the photoelectrochemical measurements were conducted under 980 nm irradiation. The photocurrent response of the as-prepared electrodes was measured to understand the photoexcited electron transfer in the $\alpha\text{-NaYF}_4\text{:Yb,Tm@TiO}_2\text{/RGO}$ composites. As shown in Fig. 6(A), the photocurrent responses for $\alpha\text{-NaYF}_4\text{:Yb,Tm@TiO}_2\text{/RGO}$ composite electrodes are prompt, steady and reproducible during repeated on/off cycles of the NIR illumination. In contrast, no photocurrent responses occurs for bare $\alpha\text{-NaYF}_4\text{:Yb,Tm}$, and much lower photocurrent density is found in the case of $\alpha\text{-NaYF}_4\text{:Yb,Tm@TiO}_2$ and $\alpha\text{-NaYF}_4\text{:Yb,Tm/TiO}_2\text{/RGO}$ mixture. The steady photocurrent density for the $\alpha\text{-NaYF}_4\text{:Yb,Tm@TiO}_2\text{/RGO}$ electrode reaches $0.3 \mu\text{A}/\text{cm}^2$, which is respectively 3.75 and 2.00 times as high as that of $\alpha\text{-NaYF}_4\text{:Yb,Tm@TiO}_2$ electrode ($0.08 \mu\text{A}/\text{cm}^2$) and $\alpha\text{-NaYF}_4\text{:Yb,Tm/TiO}_2\text{/RGO}$ mixture electrode ($0.15 \mu\text{A}/\text{cm}^2$) under the same irradiation conditions, suggesting the positive synergistic effect between $\alpha\text{-NaYF}_4\text{:Yb,Tm@TiO}_2$ and RGO in the composite. The enhancement of the photocurrent for the $\alpha\text{-NaYF}_4\text{:Yb,Tm@TiO}_2\text{/RGO}$ electrode indicates a higher photo-induced charge separation efficiency and charge transfer rate in the composite. The RGO serves as an acceptor and a transporter for the electrons generated from TiO_2 shell after excited by upconversion energy from the $\alpha\text{-NaYF}_4\text{:Yb,Tm}$ core, thus inhibiting the recombination of photo-generated electron-hole pairs effectively.

The interface charge separation efficiency was also investigated by the typical electrochemical impedance (EIS) spectra. Fig. 6(B) shows the EIS Nyquist plots of the $\alpha\text{-NaYF}_4\text{:Yb,Tm@TiO}_2$ and $\alpha\text{-NaYF}_4\text{:Yb,Tm/TiO}_2\text{/RGO}$ mixture electrodes. The $\alpha\text{-NaYF}_4\text{:Yb,Tm@TiO}_2\text{/RGO}$ electrode exhibits a smaller arc radius compared to the $\alpha\text{-NaYF}_4\text{:Yb,Tm@TiO}_2$ electrode, indicating a more efficient separation of photo-generated electron-hole pairs and a higher efficiency of charge immigration across the electrode/electrolyte interface [40].

$\alpha\text{-NaYF}_4\text{:Yb,Tm@TiO}_2\text{/RGO}$ before and after NIR irradiation. The arc radius on the EIS Nyquist plot can reflect the reaction rate on the surface of the electrode. The smaller arc radius implies a more effective separation of photo-generated electron-hole pairs and a higher efficiency of charge immigration across the electrode/electrolyte interface [40]. The arc radius of $\alpha\text{-NaYF}_4\text{:Yb,Tm@TiO}_2\text{/RGO}$ electrode is smaller than that of $\alpha\text{-NaYF}_4\text{:Yb,Tm@TiO}_2$ under both dark and light conditions, suggesting that the separation and immigration of photo-generated electron-hole pairs are more efficient on $\alpha\text{-NaYF}_4\text{:Yb,Tm@TiO}_2\text{/RGO}$ electrode, which is in good accordance with the result of the photocurrent measurement and further confirms the incorporation of RGO can promote the interface charge separation under NIR irradiation.

3.4. Photocatalytic performance

MB, MO and phenol were used as model pollutants to investigate the photocatalytic activity of the as-prepared upconversion photocatalysts under NIR irradiation of 980 nm. Before irradiation, a dark adsorption test was carried out to estimate the adsorption of these pollutants by the photocatalysts. It is found that the adsorbed MB after reaching adsorption equilibrium is about 10.7%, 45.3% and 46.4% for $\alpha\text{-NaYF}_4\text{:Yb,Tm@TiO}_2$, $\alpha\text{-NaYF}_4\text{:Yb,Tm@TiO}_2\text{/RGO}$ and $\alpha\text{-NaYF}_4\text{:Yb,Tm/TiO}_2\text{/RGO}$ mixture respectively (Fig. S2), indicating the introduction of RGO can significantly enhance the absorption ability of composite photocatalyst. In addition, similar adsorption behaviors were found for MO and phenol, except that the overall adsorption amounts follow the order of MB > MO > phenol. As known, the adsorption of dye molecules is a prerequisite for the photocatalytic dye degradation, because the photo-redox reactions usually occur on the surface of the photocatalysts [41]. Therefore, the enhanced adsorption with RGO is expected to benefit the NIR-driven photocatalytic degradation activity. It is noted that the pollutants adsorption ratio by $\alpha\text{-NaYF}_4\text{:Yb,Tm@TiO}_2\text{/RGO}$ and $\alpha\text{-NaYF}_4\text{:Yb,Tm/TiO}_2\text{/RGO}$ mixture was the same, suggesting the core-shell nanostructure of $\alpha\text{-NaYF}_4\text{:Yb,Tm@TiO}_2$ would not affect the pollutants adsorption and the enhanced adsorption capacity was due to the incorporation of RGO.

Fig. 7(A) shows the concentration changes of MB catalyzed by the as-prepared samples under NIR irradiation as a function of the irradiation time. No MB degradation is found under NIR irradiation without photocatalyst (Light control) or photocatalyst without light (Dark control). It is found that $\alpha\text{-NaYF}_4\text{:Yb,Tm}$ and $\alpha\text{-NaYF}_4\text{:Yb,Tm/RGO}$ exhibit almost no activity, while about

40.8% MB is degraded in 12 h by using $\alpha\text{-NaYF}_4\text{:Yb,Tm@TiO}_2$ as the photocatalyst, indicating the TiO_2 has a major role in the NIR-driven photocatalytic degradation process. Interestingly, the degradation ratio reaches 81.1% in the presence of $\alpha\text{-NaYF}_4\text{:Yb,Tm@TiO}_2/\text{RGO}$. Incorporation of RGO clearly demonstrates a positive effect on the enhancement of the NIR-driven photocatalytic activity. With the increase of GO addition in preparation process, the MB degradation ratio by the as-prepared $\alpha\text{-NaYF}_4\text{:Yb,Tm@TiO}_2/\text{RGO}$ first increases, and then gradually decreases (Fig. S3). The sample prepared by adding 0.6 mL GO shows the highest activity, while higher content deteriorates the photocatalytic activity, which may be due to the shielding effect of excess graphene [42,43]. However, the photo-degradation activity is much lower in the case of $\alpha\text{-NaYF}_4\text{:Yb,Tm/TiO}_2/\text{RGO}$ mixture (54.3% in degradation ratio), suggesting that the core–shell nanostructure of $\alpha\text{-NaYF}_4\text{:Yb,Tm@TiO}_2$ is also crucial for achieving a good NIR-driven photocatalytic performances. In addition, the $\alpha\text{-NaYF}_4\text{:Yb,Tm@TiO}_2/\text{RGO}$ also exhibits much enhanced photocatalytic activity towards the degradation of MO and phenol (Fig. 7(B) and (C)). It is found that the degradation ratio of MO and phenol is much lower than that of MB, probably due to the lower adsorption capacity and the different molecular structures of these pollutants.

As these pollutants cannot absorb and be excited by NIR light, the photosensitization mechanism which prevails in visible-light-driven photocatalytic dye decolorization is unlikely to occur. To verify the pollutant degradation instead of only decolorization, TOC removal efficiencies of the pollutants were tested after NIR irradiation for 12 h. It is found that the TOC removal efficiencies reach 59.2%, 45.9% and 29.8% for MB, MO and phenol, respectively, which is correspondingly higher than that of $\alpha\text{-NaYF}_4\text{:Yb,Tm@TiO}_2$ and $\alpha\text{-NaYF}_4\text{:Yb,Tm/TiO}_2/\text{RGO}$ mixture (Fig. 7(D)). Furthermore, to quantitatively understand the reaction kinetics of pollutants degradation in our experiments, we apply the pseudo-first-order model which is a widely used model to evaluate the photocatalytic degradation rate [44]. Apparent degradation rate constants (k) were calculated by plots of $-\ln(C/C_0)$ versus irradiation time, as described in Fig. S4, and the values are shown in Table S1. The results indicate that all the experiment data fit a first-order kinetic model well, and introduction of RGO in the core–shell nanostructure of $\alpha\text{-NaYF}_4\text{:Yb,Tm@TiO}_2$ significantly facilitates the degradation rate of organic pollutants. For example, the obtained k values for MB degradation is 0.1432 h^{-1} in the case of $\alpha\text{-NaYF}_4\text{:Yb,Tm@TiO}_2/\text{RGO}$, which is about 3.39 and 2.14 times higher than $\alpha\text{-NaYF}_4\text{:Yb,Tm@TiO}_2$ and $\alpha\text{-NaYF}_4\text{:Yb,Tm/TiO}_2/\text{RGO}$ mixture, respectively. Similarly, the $\alpha\text{-NaYF}_4\text{:Yb,Tm@TiO}_2/\text{RGO}$ shows enhanced activity by a factor of 2.74 and 1.52 times for MO degradation, 2.3 and 1.83 times for phenol degradation, compared with $\alpha\text{-NaYF}_4\text{:Yb,Tm@TiO}_2$ and $\alpha\text{-NaYF}_4\text{:Yb,Tm/TiO}_2/\text{RGO}$ mixture, respectively. It is worth noting that although the $\alpha\text{-NaYF}_4\text{:Yb,Tm@TiO}_2$ shows a higher upconversion UV energy transfer efficiency than that of $\alpha\text{-NaYF}_4\text{:Yb,Tm/TiO}_2/\text{RGO}$ mixture (Fig. 4), the photocatalytic activity is relatively lower. This result indicates besides upconversion UV energy transfer efficiency, the photo-induced charge separation (enhanced by incorporation of RGO) is more important for upconversion-based NIR-driven photocatalysis,

To evaluate the effective contribution of NIR-photocatalysis in the overall sunlight-driven photocatalysis, the photocatalytic degradation activity of the $\alpha\text{-NaYF}_4\text{:Yb,Tm@TiO}_2/\text{RGO}$ was also tested under simulated sunlight irradiation by using a 300 W xenon lamp with an AM 1.5 filter. As shown in Fig. 8(A), more than 90% of MB and MO, while about 61% of phenol is degraded within 1 h of simulated sunlight irradiation. In addition, the photocatalytic degradation of phenol was compared under simulated NIR irradiation by using a long-pass cutoff filter ($\lambda > 700 \text{ nm}$). Anatase TiO_2 was used as the reference photocatalyst. As shown in Fig. 8(B),

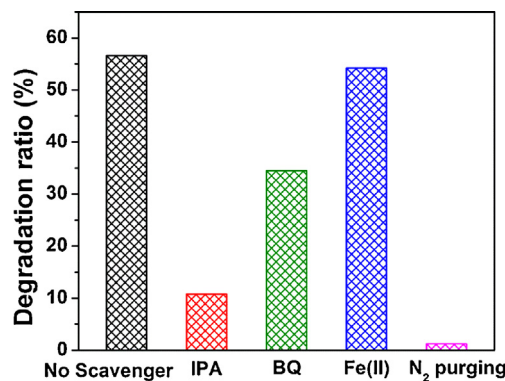


Fig. 9. NIR-driven photocatalytic degradation of MB by $\alpha\text{-NaYF}_4\text{:Yb,Tm@TiO}_2/\text{RGO}$ with different scavengers.

the $\alpha\text{-NaYF}_4\text{:Yb,Tm@TiO}_2/\text{RGO}$ exhibits much higher activity than TiO_2 , and about 36% of phenol is degraded by TiO_2 under simulated sunlight irradiation, while no activity is observed under NIR irradiation in the case of TiO_2 . Correspondingly, about 15% degradation of phenol is still degraded by using $\alpha\text{-NaYF}_4\text{:Yb,Tm@TiO}_2/\text{RGO}$ as the photocatalyst under simulated NIR irradiation. These results confirm that the enhanced activity of $\alpha\text{-NaYF}_4\text{:Yb,Tm@TiO}_2/\text{RGO}$ under sunlight irradiation is mainly due to the utilization of NIR energy.

3.5. Detection of reactive species

To identify the major reactive species, scavengers study was conducted by using isopropanol (IPA), benzoquinone (BQ), Fe(II)-EDTA and N_2 purging as $\cdot\text{OH}$, $\cdot\text{O}_2^-$, H_2O_2 and O_2 scavengers, respectively [41,45–47]. Fig. 9 shows the photo-degradation ratio of MB in the presence of different scavengers under NIR-irradiation for 6 h. It is found that ~56.6% MB degradation was achieved without adding scavengers. However, the degradation ratio decreases significantly to ~10.8% with the addition of IPA (1 mM), indicating $\cdot\text{OH}$ is the major reactive species. Meanwhile, the addition of BQ (1 mM) as $\cdot\text{O}_2^-$ scavenger is also found to inhibit the degradation ratio to ~34.5%, suggesting $\cdot\text{O}_2^-$ is also involved in the photocatalytic process. To verify the role of molecular O_2 , N_2 was purged into the system to create anaerobic conditions, and the degradation ratio was almost completely inhibited. This may be rationalized by considering the fact that $\cdot\text{O}_2^-$ and $\cdot\text{OH}$ is mainly produced from the conduction band in TiO_2 -based photocatalysts [48], and therefore, the removal of O_2 would significantly inhibit the e^- trapping by O_2 to produce $\cdot\text{O}_2^-$ and $\cdot\text{OH}$. This result also confirms that MB is degraded by photo-oxidation with the aid of molecular O_2 instead of photo-reduction or adsorption. In addition, the role of H_2O_2 was studied by using Fe(II)-EDTA (0.1 mM) as scavenger, and no changes of the degradation ratio was found, suggesting H_2O_2 may not be involved in the photocatalytic degradation process, which is consistent with previous study that photo-generated H_2O_2 is inactive for organic compounds degradation [41].

Photoluminescence method by using terephthalic acid as a $\cdot\text{OH}$ trapping agent was used to further confirm the generation of $\cdot\text{OH}$ radicals. It is known that $\cdot\text{OH}$ reacts with terephthalic acid in basic solution to generate 2-hydroxyterephthalic acid, which emits a unique fluorescence signal with its peak centered at 425 nm. As shown in Fig. 10(A), significant fluorescent signals associated with 2-hydroxyterephthalic acid are generated upon NIR irradiation of $\alpha\text{-NaYF}_4\text{:Yb,Tm@TiO}_2/\text{RGO}$ suspended in a terephthalic acid solution for different irradiation times. In addition, the amount of $\cdot\text{OH}$ radicals increase almost linearly with the irradiation time (Fig. 10(B)), suggesting the stability of the $\cdot\text{OH}$ radicals

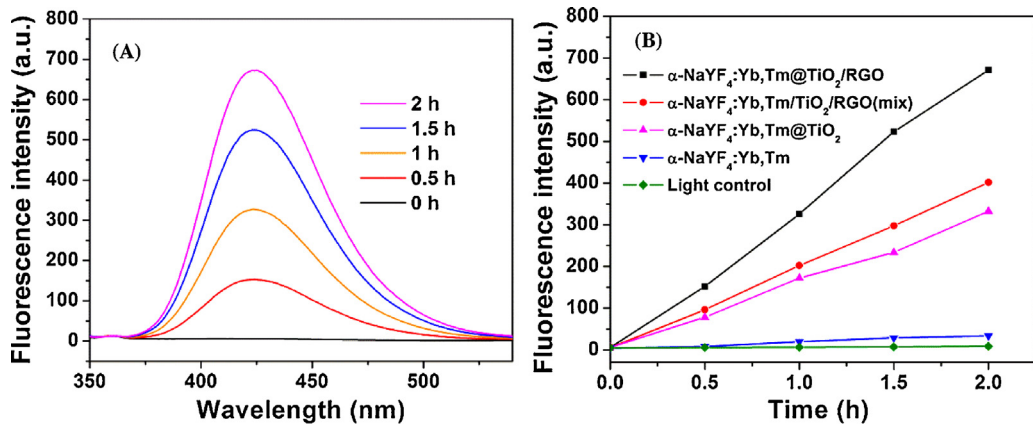


Fig. 10. (A) Fluorescence emission spectral changes observed in the presence of $\alpha\text{-NaYF}_4\text{:Yb,Tm@TiO}_2\text{/RGO}$ with NIR irradiation in a 4×10^{-4} mol/L terephthalic acid and 2×10^{-3} mol/L NaOH (excitation at 320 nm); (B) fluorescence emission intensity at 426 nm against irradiation time in the presence of different samples.

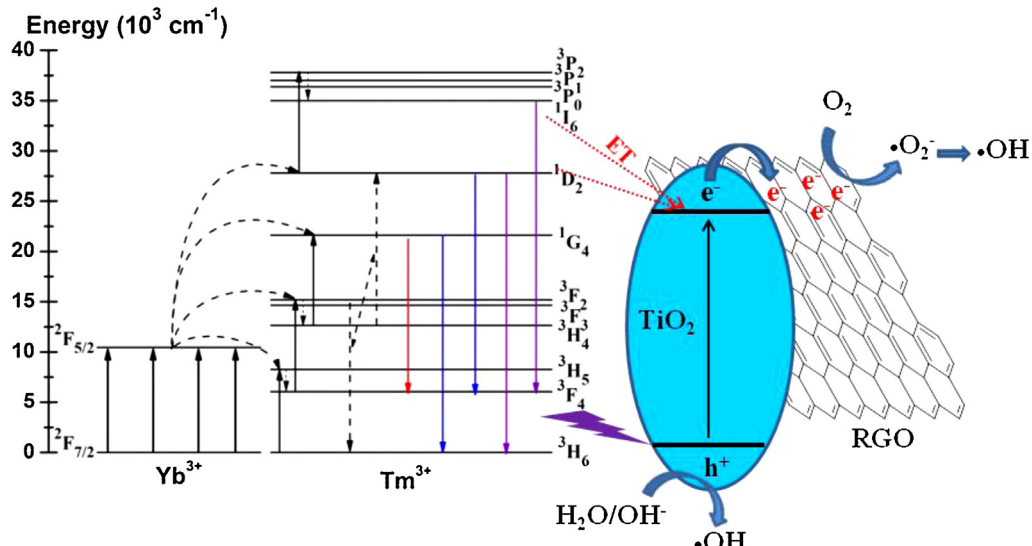


Fig. 11. Schematic illustration of the energy transfer process and the photocatalytic mechanisms for $\alpha\text{-NaYF}_4\text{:Yb,Tm@TiO}_2\text{/RGO}$ under NIR irradiation.

generation. In contrast, no capability of producing •OH radicals is observed in the case of $\alpha\text{-NaYF}_4\text{:Yb,Tm}$, while much lower amounts of •OH is produced in the case of $\alpha\text{-NaYF}_4\text{:Yb,Tm@TiO}_2$ and $\alpha\text{-NaYF}_4\text{:Yb,Tm/TiO}_2\text{/RGO}$ mixture. The •OH radicals generation activity matches well with the photocatalytic degradation activity. These results indicate that the photo-degradation is mainly driven by the •OH radicals generated during the NIR-irradiation process, and much more •OH radicals can be produced with the aid of graphene.

3.6. Photocatalytic mechanisms

Based on the above results, the mechanism for the NIR-driven photocatalysis is shown in Fig. 11. Under NIR irradiation, the pump 980 nm photons excites only the Yb³⁺ ions, and three successive energy transfers from Yb³⁺ to Tm³⁺ occur to populate the ³H₅, ³F₂, and ¹G₄ levels [49–51]. As a result, the red (¹G₄ → ³F₄) and blue (¹G₄ → ³H₆) emissions are realized. The population of the ¹D₂ level cannot be directly achieved by the fourth photon from Yb³⁺ via energy transfer to the ¹G₄ because of the large energy mismatch (about 3500 cm^{-1}) between them [52]. The cross-relaxation process of (³F₂ + ³H₄ → ³H₆ + ¹D₂) between Tm³⁺ ions may be responsible for populating the ¹D₂ level [53]. In this case, the blue (¹D₂ → ³F₄) and near ultraviolet (¹D₂ → ³H₆) emissions are

obtained. After that, the ¹D₂ state is promoted to the ³P₂ state via another energy transfer from excited Yb³⁺ and then relaxed non-radiatively to the ¹I₆ level, which subsequently gives the 350 nm ultraviolet emmissions with the transition of ⁰P₃ → ³H₆.

After excitation of the $\alpha\text{-NaYF}_4\text{:Yb,Tm}$ upconversion core, the anatase TiO₂ shell is directly excited by the energy transfer from ¹D₂ and ¹I₆ levels of Tm³⁺ ions via fluorescence resonance energy transfer (FRET) processes [14], as these two excited state levels match with the band gap of TiO₂. Consequently, the photo-generated electrons are excited from the valence band (VB) to the conduction band (CB) of TiO₂ shells, and then transfer to the RGO nanosheets because of the low Fermi energy level of RGO (−0.08 eV vs. NHE). The separated e⁻ are then trapped by O₂ to produce O₂⁻, which then generates •OH for photocatalysis. The high conductivity of RGO guarantees the enhanced interfacial charge transfer and separation, as confirmed by the photoelectrochemical EIS measurements (Fig. 6(B)). On the other hand, the photo-generated h⁺ in the valence band (VB) of TiO₂ transfers to the surface of the catalyst and can also react with H₂O/OH⁻ to produce •OH radicals.

4. Conclusions

In summary, we have demonstrated a new strategy by integrating the core–shell structure of $\alpha\text{-NaYF}_4\text{:Yb,Tm@TiO}_2$ upconversion

photocatalyst with the excellent electrical properties of graphene to for NIR-driven photocatalysis. The core–shell structure guarantees intimate interfacial contacts between α -NaYF₄:Yb,Tm and TiO₂, allowing the direct energy transfer from the excited states in upconversion core, while the incorporation of graphene in the composites facilitate not only the light and pollutants absorption, but also the interfacial charge separation efficiency. As a result, the as-prepared α -NaYF₄:Yb,Tm@TiO₂/RGO shows significantly enhanced NIR-driven photocatalytic activity than α -NaYF₄:Yb,Tm@TiO₂ and α -NaYF₄:Yb,Tm/TiO₂/RGO physical mixture towards the degradation of various organic pollutants, including MB, MO and phenol. In addition, •OH radicals are detected under NIR irradiation and proved to be the major reactive species. As a proof of concept, this study provides useful information for developing NIR-driven photocatalysis by nanostructure design combined with graphene modification.

Acknowledgment

This work was supported by the National Science Foundation of China (Ref. No.: 21173179) and a grant from the Research Grants Council of the Hong Kong Special Administrative Region, China, under Theme-based Research Scheme through Project No. T23-407/13-N.

Appendix A. Supplementary data

Supplementary data associated with this article can be found, in the online version, at <http://dx.doi.org/10.1016/j.apcatb.2015.09.022>.

References

- [1] A. Kubacka, M. Fernandez-Garcia, G. Colon, Chem. Rev. 112 (2012) 1555–1614.
- [2] I.K. Konstantinou, T.A. Albanis, Appl. Catal. B Environ. 49 (2004) 1–14.
- [3] X. Chen, S. Shen, L. Guo, S.S. Mao, Chem. Rev. 110 (2010) 6503–6570.
- [4] G.D. Yang, Z. Jiang, H.H. Shi, T.C. Xiao, Z.F. Yan, J. Mater. Chem. 20 (2010) 5301–5309.
- [5] H.X. Li, Z.F. Bian, J. Zhu, Y.N. Huo, H. Li, Y.F. Lu, J. Am. Chem. Soc. 129 (2007) 4538–4539.
- [6] J.H. Xu, J.X. Li, W.L. Dai, Y. Cao, H.X. Li, K.N. Fan, Appl. Catal. B Environ. 79 (2008) 72–80.
- [7] X. Zhang, L.Z. Zhang, T.F. Xie, D.J. Wang, J. Phys. Chem. C 113 (2009) 7371–7378.
- [8] C. Zhen, L.Z. Wang, L. Liu, G. Liu, G.Q. Lu, H.M. Cheng, Chem. Commun. 49 (2013) 6191–6193.
- [9] L. Zeng, Z. Lu, J. Yang, M.H. Li, W.L. Song, C.S. Xie, Appl. Catal. B Environ. 166 (2015) 1–8.
- [10] C.C. Chen, W.H. Ma, J.C. Zhao, Chem. Soc. Rev. 39 (2010) 4206–4219.
- [11] X. Huang, S. Han, W. Huang, X. Liu, Chem. Soc. Rev. 42 (2013) 173–201.
- [12] Y.W. Zhang, Z.L. Hong, Nanoscale 5 (2013) 8930–8933.
- [13] W.P. Qin, D.S. Zhang, D. Zhao, L.L. Wang, K.Z. Zheng, Chem. Commun. 46 (2010) 2304–2306.
- [14] Y.N. Tang, W.H. Di, X.S. Zhai, R.Y. Yang, W.P. Qin, ACS Catal. 3 (2013) 405–412.
- [15] S. Stankovich, D.A. Dikin, G.H.B. Dommett, K.M. Kohlhaas, E.J. Zimney, E.A. Stach, R.D. Piner, S.T. Nguyen, R.S. Ruoff, Nature 442 (2006) 282–286.
- [16] J.C. Meyer, A.K. Geim, M.I. Katsnelson, K.S. Novoselov, T.J. Booth, S. Roth, Nature 446 (2007) 60–63.
- [17] T.G. Xu, L.W. Zhang, H.Y. Cheng, Y.F. Zhu, Appl. Catal. B Environ. 101 (2011) 382–387.
- [18] Q.J. Xiang, J.G. Yu, M. Jaroniec, Chem. Soc. Rev. 41 (2012) 782–796.
- [19] Q. Li, B.D. Guo, J.G. Yu, J.R. Ran, B.H. Zhang, H.J. Yan, J.R. Gong, J. Am. Chem. Soc. 133 (2011) 10878–10884.
- [20] H. Zhang, X.J. Lv, Y.M. Li, Y. Wang, J.H. Li, ACS Nano 4 (2010) 380–386.
- [21] Z. Li, C. Li, Y. Mei, L. Wang, G. Du, Y. Xiong, Nanoscale 5 (2013) 3030–3036.
- [22] D.X. Xu, Z.W. Lian, M.L. Fu, B.L. Yuan, J.W. Shi, H.J. Cui, Appl. Catal. B Environ. 142 (2013) 377–386.
- [23] W. Wang, M.Y. Ding, C.H. Lu, Y.R. Ni, Z.Z. Xu, Appl. Catal. B Environ. 144 (2014) 379–385.
- [24] X.Q. An, J.C. Yu, RSC Adv. 1 (2011) 1426–1434.
- [25] L. Ren, X. Qi, Y.D. Liu, Z.Y. Huang, X.L. Wei, J. Li, L.W. Yang, J.X. Zhong, J. Mater. Chem. 22 (2012) 11765–11771.
- [26] W. Wang, W.J. Huang, Y.R. Ni, C.H. Lu, L.J. Tan, Z.G. Xu, Appl. Surf. Sci. 282 (2013) 832–837.
- [27] Y.C. Li, L. Zhang, Z.F. Hu, J.C. Yu, Nanoscale 7 (2015) 10896–10902.
- [28] Y.J. Sun, Y. Chen, L.J. Tian, Y. Yu, X.G. Kong, J.W. Zhao, H. Zhang, Nanotechnology 18 (2007) 275609.
- [29] W.J. Wang, Y. Yu, T.C. An, G.Y. Li, H.Y. Yip, J.C. Yu, P.K. Wong, Environ. Sci. Technol. 46 (2012) 4599–4606.
- [30] W.G. Wang, J.G. Yu, Q.J. Xiang, B. Cheng, Appl. Catal. B Environ. 119–120 (2012) 109–116.
- [31] X.H. Li, J.S. Chen, X.C. Wang, M.E. Schuster, R. Schlögl, M.A. Antonietti, ChemSusChem 5 (2012) 642–646.
- [32] W.J. Wang, J.C. Yu, D.H. Xia, P.K. Wong, Y.C. Li, Environ. Sci. Technol. 47 (2013) 8724–8732.
- [33] G.S. Yi, G.M. Chow, Adv. Funct. Mater. 16 (2006) 2324–2329.
- [34] T. Jiang, W.P. Qin, W.H. Di, R.Y. Yang, D.M. Liu, X.S. Zhai, G.S. Qin, CrystEngComm 14 (2012) 2302–2307.
- [35] Y.S. Liu, D.T. Tu, H.M. Zhu, R.F. Li, W.Q. Luo, X.Y. Chen, Adv. Mater. 22 (2010) 3266–3271.
- [36] W.L. Ren, G. Tian, S. Jian, Z.J. Gu, L.J. Zhou, L. Yan, S. Jin, W.Y. Yin, Y.L. Zhao, RSC Adv. 2 (2012) 7037–7041.
- [37] D. Zhang, D. Zhao, K. Zheng, N. Liu, W. Qin, J. Nanosci. Nanotechnol. 11 (2011) 9761–9764.
- [38] C. Li, F. Wang, J. Zhu, J.C. Yu, Appl. Catal. B Environ. 100 (2010) 433–439.
- [39] K. Turcheniuk, C.H. Hage, J. Spadavecchia, A.Y. Serrano, I. Larroulet, A. Pesquera, A. Zurutuza, M.G. Pisfil, L. Héliot, J. Boukaert, R. Boukherroub, S. Szunerits, J. Mater. Chem. B 3 (2015) 375–386.
- [40] S.J. Hong, S. Lee, J.S. Jang, J.S. Lee, Energ. Environ. Sci. 4 (2011) 1781–1787.
- [41] W.J. Wang, L.S. Zhang, T.C. An, G.Y. Li, H.Y. Yip, P.K. Wong, Appl. Catal. B Environ. 108–109 (2011) 108–116.
- [42] Q. Li, B.D. Guo, J.G. Yu, J.R. Ran, B.H. Zhang, H.J. Yan, J.R. Gong, J. Am. Chem. Soc. 133 (2011) 10878–10884.
- [43] X.Q. An, J.C. Yu, F. Wang, C.H. Li, Y.C. Li, Appl. Catal. B Environ. 129 (2013) 80–88.
- [44] W.J. Wang, X.Q. Chen, G. Liu, Z.R. Shen, D.H. Xia, P.K. Wong, J.C. Yu, Appl. Catal. B Environ. 176–177 (2015) 444–453.
- [45] L.S. Chang, K.H. Wong, H.Y. Yip, C. Hu, J.C. Yu, C.Y. Chan, P.K. Wong, Environ. Sci. Technol. 44 (2010) 1392–1398.
- [46] Y.X. Chen, S.Y. Yang, K. Wang, L.P. Lou, J. Photochem. Photobiol. A 172 (2005) 47–54.
- [47] A.A. Khodja, A. Boulkamh, C. Richard, Appl. Catal. B Environ. 59 (2005) 147–154.
- [48] Y. Kikuchi, K. Sunada, T. Iyoda, K. Hashimoto, A. Fujishima, J. Photochem. Photobiol. A 106 (1997) 51–56.
- [49] X. Chen, W.J. Wang, X.Y. Chen, J.H. Bi, L. Wu, Z.H. Li, X.Z. Fu, Mater. Lett. 63 (2009) 1023–1026.
- [50] F. Zhang, Y.F. Shi, X.H. Sun, D.Y. Zhao, G.D. Stucky, Chem. Mater. 21 (2009) 5237–5243.
- [51] J. Yang, C.M. Zhang, C. Peng, C.X. Li, L.L. Wang, R.T. Chai, J. Lin, Chem. Eur. J. 15 (2009) 4649–4655.
- [52] G.S. Qin, W.P. Qin, C.F. Wu, S.H. Huang, J.S. Zhang, S.Z. Lu, D. Zhao, H.Q. Liu, J. Appl. Phys. 99 (2003) 1–3.
- [53] G. De, W. Qin, J. Zhang, J. Zhang, Y. Wang, C. Cao, Y. Cui, J. Lumin. 122 (2007) 128–130.